

# Dynamical singularity of the rate function for quench dynamics in finite-size quantum systems

Yumeng Zeng,<sup>1,2</sup> Bozhen Zhou,<sup>1</sup> and Shu Chen<sup>1,2,3,\*</sup>

<sup>1</sup>*Beijing National Laboratory for Condensed Matter Physics,  
Institute of Physics, Chinese Academy of Sciences, Beijing 100190, China*

<sup>2</sup>*School of Physical Sciences, University of Chinese Academy of Sciences, Beijing 100049, China*

<sup>3</sup>*Yangtze River Delta Physics Research Center, Liyang, Jiangsu 213300, China*

(Dated: April 11, 2023)

The dynamical quantum phase transition is characterized by the emergence of nonanalytic behaviors in the rate function, corresponding to the occurrence of exact zero points of the Loschmidt echo in the thermodynamical limit. In general, exact zeros of the Loschmidt echo are not accessible in a finite-size quantum system except for some fine-tuned quench parameters. In this work, we study the realization of the dynamical singularity of the rate function for finite-size systems under the twist boundary condition, which can be introduced by applying a magnetic flux. By tuning the magnetic flux, we illustrate that exact zeros of the Loschmidt echo can be always achieved when the postquench parameter is across the underlying equilibrium phase transition point, and thus the rate function of a finite-size system is divergent at a series of critical times. We demonstrate our theoretical scheme by calculating the Su-Schrieffer-Heeger model and the Creutz model in detail and exhibit its applicability to more general cases. Our result unveils that the emergence of dynamical singularity in the rate function can be viewed as a signature for detecting dynamical quantum phase transition in finite-size systems. We also unveil that the critical times in our theoretical scheme are independent on the systems size, and thus it provides a convenient way to determine the critical times by tuning the magnetic flux to achieve the dynamical singularity of the rate function.

## I. INTRODUCTION

Since the dynamical quantum phase transition (DQPT) was proposed<sup>1</sup>, it has become an important concept in describing a class of nonequilibrium critical phenomena associated with singular behavior in the real-time evolution of the Loschmidt echo (LE)<sup>1-21</sup>. Given  $\langle \psi_i | \psi(t) \rangle$  denotes the overlap of an initial ground state  $|\psi_i\rangle$  and its time evolution state  $|\psi(t)\rangle = e^{-iH_f t} |\psi_i\rangle$  governed by a postquench Hamiltonian  $H_f$ , the LE is defined as

$$\mathcal{L}(t) = |\langle \psi_i | \psi(t) \rangle|^2, \quad (1)$$

which represents the return probability of the time evolution state to the initial state<sup>22</sup>. The LE plays a particularly important role in the characterization of the DQPT<sup>20,21</sup>. When the phase-driving parameter is quenched across an underlying equilibrium phase transition point, a series of zero points of LE emerge at some critical times. In general, exact zeros of LE only occur when the system size tends to infinity<sup>1,23,24</sup>. Meanwhile, LE always approaches zero in the thermodynamical limit, even when the quench parameter does not cross the transition point. This can be attributed to the Anderson orthogonality catastrophe<sup>25</sup> for the reason that the multiplication of an infinite number of numbers with magnitude less than 1 equals 0. To eliminate the effect of system size properly, it is convenient to introduce the rate function of LE given by

$$\lambda(t) = -\frac{1}{L} \ln \mathcal{L}(t). \quad (2)$$

As the LE is analogous to a dynamical boundary partition function, the rate function  $\lambda(t)$  can be viewed as a dynamical free energy. Thus the DQPT is characterized by nonanalytic behaviors in the rate function of LE in the thermodynamical limit.

According to the theory of DQPT, the nonanalyticity of rate function occurs at the critical times  $t_n^*$  when the quench parameter is across the equilibrium phase transition point, corresponding to the emergence of exact zeros of LE in the thermodynamical limit. For finite size systems, LE usually has no exact zeros, except for fine-tuned post-quench parameters which fulfill specific constraint conditions<sup>24</sup>. Therefore, to study the DQPT and extract the critical times in finite-size quantum systems, one needs to resort to finite-size analysis to extract the non-analytical properties and critical times in the limit of  $L \rightarrow \infty$ . With the increase of  $L$ ,  $\mathcal{L}(t)$  approaches zero at critical times  $t_n^*$ , and thus  $\ln \mathcal{L}(t_n^*) \rightarrow \infty$  when  $L \rightarrow \infty$ . However,  $\lambda(t_n^*)$  is not divergent and only displays a cusp due to the fact that the divergence is offset by the  $L$  in the denominator. For a finite system with size  $L$ ,  $t_n^*(L)$  are determined by the times at which  $\lambda$  takes the local maximum. As we shall demonstrate later,  $t_n^*(L)$  does not fulfill a simple fitting relation with  $L$ . Thanks to the advance of quantum simulators, quantum simulations of DQPT were already reported in various systems<sup>26-33</sup>, such as trapped ions<sup>26,27</sup>, Rydberg atoms<sup>28</sup>, and ultracold atoms<sup>29-31</sup>, with finite sizes. Therefore, extracting the non-analytical signature of DQPT in finite-size systems is important from both experimental and theoretical aspects.

In this work, we study the non-analytical behaviors of DQPT in finite-size systems with a twist boundary condi-

tion which can be realized by introducing a magnetic flux  $\phi_c$  into the periodic system. When the quench parameter is across the equilibrium phase transition point, by tuning the flux, we demonstrate that exact zeros of LE can be always achieved at critical times  $t_n^*$  even for a finite-size system. It is interesting that the critical times obtained in this way are independent of the system sizes and match exactly with the critical times obtained in the thermodynamical limit of the corresponding periodic system. Due to the finite size  $L$ , the rate function  $\lambda(t)$  should be divergent at critical times  $t_n^*$ , corresponding to the exact zeros of LE. On the other hand, no exact zeros can be achieved if there is no DQPT, when the postquench and prequench parameters are in the same region of phases. Correspondingly, the rate function is not sensitive to the flux and does not show any singular behavior. Our theoretical work unveils that the emergence of the dynamical singularity in the rate function can be viewed as a signature for detecting DQPT in finite-size systems. Since the critical times in our theoretical scheme are not dependent on the systems size, it provides us a convenient way to determine the critical times in finite-size systems.

## II. MODELS AND SCHEME FOR ACHIEVING THE DYNAMICAL SINGULARITY

To illustrate how the singularity of the rate function arises as a result of the emergence of zero points of LE, we consider general one-dimensional (1D) two-band systems with the Hamiltonian in momentum space described by

$$\hat{h}(\gamma, k) = \sum_{\alpha=x,y,z} d_{\alpha}(\gamma, k) \hat{\sigma}_{\alpha} + d_0(\gamma, k) \hat{\mathbb{1}}, \quad (3)$$

where  $\gamma$  denotes a phase transition driving parameter;  $\hat{\sigma}_{\alpha}$  are Pauli matrices with  $\alpha = x, y, z$ ;  $d_{\alpha}(\gamma, k)$  and  $d_0(\gamma, k)$  are the corresponding vector components of  $\hat{h}(\gamma, k)$ ; and  $\hat{\mathbb{1}}$  is the unit matrix. Such systems are widely studied in the literature<sup>9–11</sup> and include, e.g., the transverse-field Ising model, quantum  $XY$  model, the Su-Schrieffer-Heeger (SSH) model, and Creutz model, as special cases. Consider a quench process described by a sudden change of driving parameter  $\gamma = \gamma_i \theta(-t) + \gamma_f \theta(t)$  with the initial state prepared as the ground state of the prequench Hamiltonian  $H(\gamma_i)$ . The LE following the quench can be written as

$$\mathcal{L} = \prod_k \mathcal{L}_k = \prod_k \left| \langle \psi_k^i | e^{-i\hat{h}(\gamma_f, k)t} | \psi_k^i \rangle \right|^2, \quad (4)$$

where  $\hat{h}(\gamma_f, k)$  is the postquench Hamiltonian with mode  $k$ . Choosing  $|\psi_k^i\rangle$  as the  $k$ -mode of the ground state of the prequench Hamiltonian, then we have

$$\mathcal{L}_k = 1 - \Lambda_k \sin^2[\epsilon_f(k)t], \quad (5)$$

with

$$\Lambda_k = 1 - \left[ \frac{\sum_{\alpha=x,y,z} d_{\alpha}(\gamma_i, k) d_{\alpha}(\gamma_f, k)}{\epsilon_i(k) \epsilon_f(k)} \right]^2,$$

where  $\epsilon_i(k) = \sqrt{\sum_{\alpha} d_{\alpha}^2(\gamma_i, k)}$  and  $\epsilon_f(k) = \sqrt{\sum_{\alpha} d_{\alpha}^2(\gamma_f, k)}$ . The singularity of rate function  $\lambda(t) = -\frac{1}{t} \ln \mathcal{L}(t)$  occurs when  $\mathcal{L}(t) = 0$ , which needs at least one  $k$ -mode fulfilling  $\Lambda_k = 1$  and gives rise to the following constraint relation

$$\sum_{\alpha=x,y,z} d_{\alpha}(\gamma_i, k) d_{\alpha}(\gamma_f, k) = 0. \quad (6)$$

To make our discussion concrete, we consider the SSH model<sup>34</sup> and the Creutz model<sup>35</sup> as examples and show the details of the calculation in this section.

### A. SSH model

First, we consider the SSH model with the vector components of Hamiltonian given by

$$d_x(k) = J_1 + J_2 \cos k, \quad (7)$$

$$d_y(k) = -J_2 \sin k \quad (8)$$

and  $d_z(k) = d_0(k) = 0$ , where  $J_1$  and  $J_2$  represent the intracellular and intercellular tunneling amplitudes, respectively. The SSH model possesses two topologically different phases for  $J_2 > J_1$  and  $J_2 < J_1$  with a phase transition occurring at the transition point of  $J_{2c}/J_1 = 1$ <sup>34,36</sup>. Then we quench parameter  $J_2$  from  $J_{2i}$  to  $J_{2f}$  at  $t = 0$  and get the LE of the SSH model

$$\mathcal{L}(t) = \prod_k \{1 - \Lambda_k \sin^2[\epsilon_f(k)t]\}, \quad (9)$$

where  $\epsilon_f(k)$  and  $\Lambda_k$  are given by

$$\epsilon_f(k) = J_1 \sqrt{1 + 2\gamma_f \cos k + \gamma_f^2}, \quad (10)$$

$$\Lambda_k = 1 - \frac{[1 + (\gamma_i + \gamma_f) \cos k + \gamma_i \gamma_f]^2}{(1 + 2\gamma_i \cos k + \gamma_i^2)(1 + 2\gamma_f \cos k + \gamma_f^2)}. \quad (11)$$

Here  $\gamma_i = \frac{J_{2i}}{J_1}$  and  $\gamma_f = \frac{J_{2f}}{J_1}$ . For convenience, we shall fix  $J_1 = 1$  and take it as the energy unit in the following calculation. For a finite size system under the periodic boundary condition (PBC), the momentum  $k$  takes discrete values  $k = 2\pi m/L$  with  $m = -L/2, -L/2 + 1, \dots, L/2 - 1$  if  $L$  is even or  $m = -(L-1)/2, -(L-1)/2 + 1, \dots, (L-1)/2$  if  $L$  is odd.

For a finite-size system under the PBC, we can utilize Eqs. (2) and (9) to calculate the rate function numerically. In Fig. 1(a), we display the rate function  $\lambda(t)$  versus time  $t$  for different system sizes  $L$ . Around the critical times  $t_n^*$ , the rate function exhibits a series of peaks and the times  $t_n^*(L)$  corresponding to these local maximums can be used to interpolate numerically the values of critical times in the limit of  $L \rightarrow \infty$ . When we increase the size,  $t_n^*(L)$  does not change linearly with  $L$ , but approaches the critical times  $t_n^*$  in an oscillating way as shown in Figs. 1(b) and 1(c). In the thermodynamical

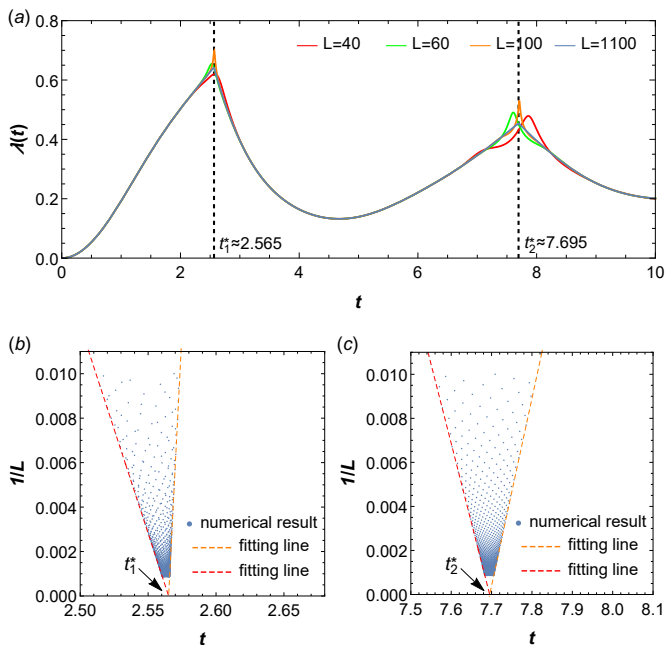


Figure 1. (a) The rate function  $\lambda(t)$  of the SSH model versus  $t$  for different system sizes  $L = 40, 60, 100$  and  $1100$ . Vertical dashed lines guide the values of critical times  $t_1^* \approx 2.565$  and  $t_2^* \approx 7.695$ . (b), (c) are numerical results of the time when  $\lambda$  takes its local maximums for different sizes  $L$ . We take  $\gamma_i = 1.5$  and  $\gamma_f = 0.5$ .

limit, the non-analytical behaviors of  $\lambda(t)$  are characterized by the emergence of a cusp at  $t_n^*$ . Using  $\lambda_{\max}$  to represent the first local maximum of  $\lambda(t)$ , we find that the value of  $\lambda_{\max}$  does not increase linearly with the increase of system size but approaches a finite number in an oscillating way. Our numerical result unveils  $\lambda_{\max} \sim 0.643$  with  $L \rightarrow \infty$ . In the thermodynamical limit  $L \rightarrow \infty$ , the momentum  $k$  distributes continuously and we have

$$\lambda(t) = -\frac{1}{2\pi} \int_0^{2\pi} \ln[1 - \Lambda_k \sin^2[\epsilon_f(k)t]] dk,$$

from which we numerically evaluate the value  $\lambda(t_1^*) \approx 0.643$  at the critical time  $t_1^*$ . It is evident that  $\lambda(t_1^*)$  is equal to  $\lambda_{\max}$  in the thermodynamical limit.

The non-analytical behaviors of the rate function occurring at the critical times  $t_n^*$  are associated to the emergence of zeros of LE. We notice that the constraint relation for ensuring  $\mathcal{L}(t) = 0$  is

$$\gamma_f = -\frac{1 + \gamma_i \cos k}{\gamma_i + \cos k}. \quad (12)$$

If  $|\gamma_i| < 1$ , Eq. (12) is fulfilled only for  $|\gamma_f| > 1$ . On the other hand, if  $|\gamma_i| > 1$ , Eq. (12) is fulfilled only for  $|\gamma_f| < 1$ . It means that the exact zeros of LE emerge only when the quench parameter  $\gamma$  is across the underlying phase transition point. When  $\gamma_i$  and  $\gamma_f$  are in different phase regions, there always exists a pair of momentum

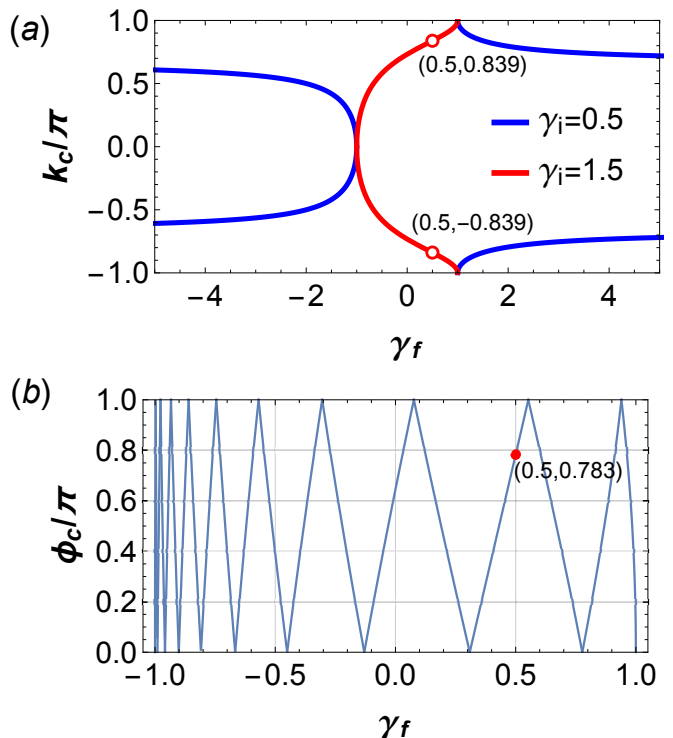


Figure 2. (a) The images of  $k_{c,+}/\pi$  and  $k_{c,-}/\pi$  versus  $\gamma_f$  for the SSH model. The blue and red lines correspond to  $\gamma_i = 0.5$  and  $\gamma_i = 1.5$ , respectively. The two red circles denote  $k_{c,+}/\pi \approx 0.839$  and  $k_{c,-}/\pi \approx -0.839$  for  $\gamma_i = 1.5$  and  $\gamma_f = 0.5$ , respectively. (b) The exact solution of  $\phi_c/\pi$  for  $\gamma_f \in [-1, 1]$ . The red point denotes  $\phi_c/\pi \approx 0.783$  for  $\gamma_f = 0.5$ . Here  $\gamma_i = 1.5$  and  $L = 20$ .

modes given by

$$k_{c,\pm} = \pm \arccos \left[ -\frac{1 + \gamma_i \gamma_f}{\gamma_i + \gamma_f} \right], \quad (13)$$

which leads to the occurrence of a series of zero points of LE at

$$t_n^* = \frac{\pi}{2\epsilon_f(k_{c,\pm})} (2n - 1), \quad (14)$$

with

$$\epsilon_f(k_{c,\pm})/J_1 = \sqrt{\frac{(1 - \gamma_f^2)(\gamma_i - \gamma_f)}{\gamma_i + \gamma_f}}, \quad (15)$$

and  $n$  being a positive integer. Since  $\epsilon_f(k_{c,+}) = \epsilon_f(k_{c,-})$ , we omit the subscript  $\pm$  in  $t_n^*$  as either  $\epsilon_f(k_{c,+})$  or  $\epsilon_f(k_{c,-})$  gives the same contribution to critical times. In Fig. 2(a), we exhibit the images of  $k_{c,+}/\pi$  and  $k_{c,-}/\pi$  versus  $\gamma_f$  for  $\gamma_i = 0.5$  and  $\gamma_i = 1.5$  according to Eq. (13), and the two red circles denote  $k_{c,+}/\pi \approx 0.839$  and  $k_{c,-}/\pi \approx -0.839$  for  $\gamma_i = 1.5$  and  $\gamma_f = 0.5$ . For finite size systems,  $k$  takes discrete values. According to Eq. (13),  $k_{c,\pm}$  is usually not equal to the quantized momentum values  $k = 2\pi m/L$  enforced by the PBC except for

some fine-tuned postquench parameters<sup>24</sup>. With the increase in the system size,  $k_{c,\pm}$  can be approached in terms of  $\min |k - k_{c,\pm}| \leq \pi/L$ , and thus exact zeros of LE are usually only achievable in the thermodynamical limit of  $L \rightarrow \infty$ .

Although exact zeros of LE for a finite-size system generally do not exist, next we unveil that exact zeros of LE can be achieved even in a finite-size system if we introduce a magnetic flux  $\phi$  into the system. The effect of magnetic flux is effectively described by the introduction of a twist boundary condition in real space  $c_{L+1}^\dagger = c_1^\dagger e^{i\phi}$  ( $\phi \in (0, \pi)$ ). Under the twist boundary condition, the quantized momentum is shifted by a factor  $\phi/L$ , i.e.,  $k = \frac{2\pi m + \phi}{L}$  with  $m = -L/2, -L/2 + 1, \dots, L/2 - 1$  if  $L$  is even or  $m = -(L-1)/2, -(L-1)/2 + 1, \dots, (L-1)/2$  if  $L$  is odd. Therefore, for a given lattice size  $L$  we can always achieve  $k_{c,+}$  or  $k_{c,-}$  by tuning the flux  $\phi$  to

$$\phi_c = \min\{\text{mod}[Lk_{c,+}, 2\pi], \text{mod}[Lk_{c,-}, 2\pi]\}. \quad (16)$$

In Fig. 2(b), we display the image of  $\phi_c/\pi$  versus  $\gamma_f$  according to Eq. (16) for the system with  $\gamma_i = 1.5$  and  $L = 20$ , and the red point in the picture denotes  $\phi_c/\pi \approx 0.783$  for  $\gamma_i = 1.5$  and  $\gamma_f = 0.5$ .

Let  $\Delta = \phi - \phi_c$ , at the time  $t = t_n^*$ , we can get

$$\lambda(t_n^*) = -\frac{1}{L}[\ln \mathcal{L}_{k^*}(t_n^*) + \sum_{k \neq k^*} \ln \mathcal{L}_k(t_n^*)], \quad (17)$$

where  $\mathcal{L}_{k^*}(t_n^*)$  comes from the contribution of the  $k^*$ -mode which is closest to  $k_c$ , i.e.,  $k^* = k_c + \Delta/L$ . Let  $\Delta \rightarrow 0$ , we can get

$$\mathcal{L}_{k^*}(t_n^*) \approx \frac{(\gamma_i + \gamma_f)^3 + \gamma_f^2 t_n^{*2} (\gamma_f - \gamma_i)(1 - \gamma_i^2)}{(\gamma_f - \gamma_i)^2 (\gamma_f + \gamma_i) L^2} \Delta^2. \quad (18)$$

When  $\Delta \rightarrow 0$ ,  $\mathcal{L}_{k^*}(t_n^*) \rightarrow 0$  and thus  $\ln \mathcal{L}_{k^*}(t_n^*)$  is divergent, i.e., when  $\phi$  achieves  $\phi_c$ , the rate function becomes divergent at the critical times.

In Fig. 3(a), we demonstrate rate functions versus  $t$  for various  $\phi$  with  $L = 20$ ,  $\gamma_i = 1.5$  and  $\gamma_f = 0.5$ . It is shown that the rate function is divergent at the critical times  $t_1^* \approx 2.565$  and  $t_2^* \approx 7.695$  when  $\phi$  is tuned to the critical value  $\phi_c$  which is shown in Fig. 2(b). In comparison with Fig. 1(a), both the nonanalytical behaviors occur at the same critical times  $t_1^*$  and  $t_2^*$ . While the nonanalyticity of the rate function in the thermodynamical limit is characterized by a cusp or a kink, the nonanalyticity of the rate function of a finite-size system induced by tuning the flux  $\phi$  is characterized by the appearance of singularity at the critical times. Such a singularity of the rate function for the finite-size system is a kind of dynamical singularity, which corresponds to the occurrence of exact zeros of LE. The existence of dynamical singularity for a finite-size system means that the initial state can evolve to its orthogonal state at a series of time by tuning the magnetic flux.

For a given  $\gamma_i$  and  $\gamma_f$ , tuning  $\phi$  from 0 to  $\pi$ , from Fig. 3(b) we can see that if  $\gamma_i$  and  $\gamma_f$  belong to the same phase,

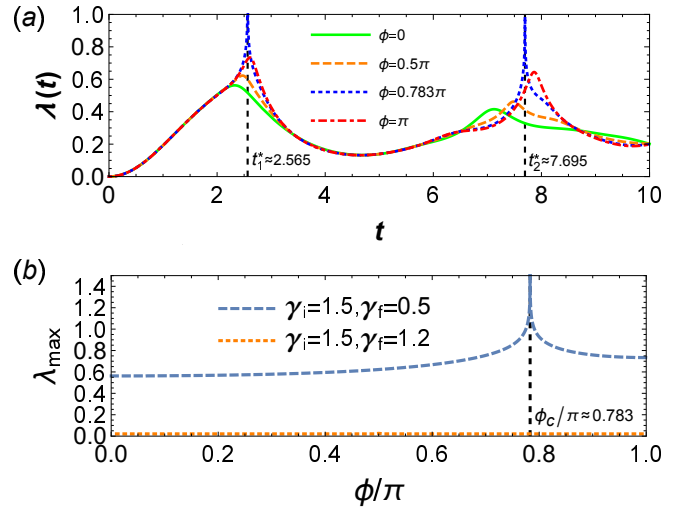


Figure 3. (a) The rate function  $\lambda(t)$  versus  $t$  for the SSH model with  $\gamma_i = 1.5$ ,  $\gamma_f = 0.5$ ,  $\phi = 0, 0.5\pi, 0.783\pi$  and  $\pi$ . Vertical dashed lines guide the divergent points  $t_1^* \approx 2.565$  and  $t_2^* \approx 7.695$ , respectively. (b) The images of  $\lambda_{\max}$  versus  $\phi/\pi$ . The dashed blue line corresponds to  $\gamma_i = 1.5$ ,  $\gamma_f = 0.5$ , whereas the dotted orange line corresponds to  $\gamma_i = 1.5$ ,  $\gamma_f = 1.2$ . The vertical dashed line guides the divergent point  $\phi_c/\pi \approx 0.783$ . Here we take  $L = 20$ .

$\lambda_{\max}$  barely changes with  $\phi$ , which means no singularity of rate function can be observed; if  $\gamma_i$  and  $\gamma_f$  belong to different phases,  $\lambda_{\max}$  will diverge at  $\phi_c/\pi \approx 0.783$ , which gives a signal of DQPT. Therefore, we can judge whether a DQPT happens by observing the change of  $\lambda_{\max}$  as a function of  $\phi$ , which continuously varies from 0 to  $\pi$ . By tuning  $\phi$  in finite-size systems, we also obtain the critical times of DQPT, which are usually defined in the thermodynamical limit and can be extracted from the finite-size-scaling analysis in previous studies.

## B. Creutz model

Next we consider the Creutz model<sup>35</sup> which describes the dynamics of a spinless electron moving in a ladder system governed by the Hamiltonian:

$$H = - \sum_{j=1} [J_h (e^{i\theta} c_{j+1}^{p\dagger} c_j^p + e^{-i\theta} c_{j+1}^{q\dagger} c_j^q) + J_d (c_{j+1}^{p\dagger} c_j^q + c_{j+1}^{q\dagger} c_j^p) + J_v c_j^{q\dagger} c_j^p + \text{H.c.}], \quad (19)$$

where  $c_j^{p(q)\dagger}$  and  $c_j^{p(q)}$  are fermionic creation and annihilation operators on the  $j$ th site of the lower (upper) chain;  $J_h$ ,  $J_d$ , and  $J_v$  represent hopping amplitudes for horizontal, diagonal, and vertical bonds, respectively; and  $\theta \in [-\pi/2, \pi/2]$  represents the magnetic flux per plaquette induced by a magnetic field piercing the ladder<sup>35,37</sup>. Via the Fourier transformation, the vector components of the Hamiltonian in momentum space

can be expressed as  $d_x(k) = -2J_d \cos k - J_v$ ,  $d_y(k) = 0$ ,  $d_z(k) = -2J_h \sin k \sin \theta$ , and  $d_0(k) = -2J_h \cos k \cos \theta$ . For simplicity, in the following we will focus on the case of  $J_h = J_d = J$  and  $J_v/2J < 1$ , and take  $J = 1$  as the unit of energy. In this case, the Creutz model has two distinct topologically nontrivial phases for  $-\pi/2 \leq \theta < 0$  and  $0 < \theta \leq \pi/2$  with a phase transition occurring at the transition point of  $\theta = 0$ <sup>38</sup>. Then we quench parameter  $\theta$  from  $\theta_i$  to  $\theta_f$  at  $t = 0$  and get the LE of the Creutz model

$$\mathcal{L}(t) = \prod_k \{1 - \Lambda_k \sin^2[\epsilon_f(k)t]\}, \quad (20)$$

where

$$\Lambda_k = 1 - \frac{16J^4[(\cos k + \tilde{J}_v)^2 + \sin^2 k \sin \theta_i \sin \theta_f]^2}{\epsilon_i^2(k)\epsilon_f^2(k)}, \quad (21)$$

$$\epsilon_i(k) = 2J\sqrt{(\cos k + \tilde{J}_v)^2 + \sin^2 k \sin^2 \theta_i}, \quad (22)$$

and

$$\epsilon_f(k) = 2J\sqrt{(\cos k + \tilde{J}_v)^2 + \sin^2 k \sin^2 \theta_f} \quad (23)$$

with  $\tilde{J}_v = J_v/2J$ . The corresponding constraint relation of Eq. (6) for the occurrence of exact zeros of LE is

$$\sin \theta_f = -\frac{(\cos k + \tilde{J}_v)^2}{\sin^2 k \sin \theta_i}. \quad (24)$$

If  $\sin \theta_i < 0$ , Eq. (24) is fulfilled only for  $\sin \theta_f > 0$ . On the other hand, if  $\sin \theta_i > 0$ , Eq. (24) is fulfilled only for  $\sin \theta_f < 0$ . It means that the dynamical singularity of the rate function exists only when the quench parameter  $\theta$  is across the underlying phase transition.

When  $\theta_i$  and  $\theta_f$  are in different phase regions, there are always two pairs of momentum modes given by

$$k_{c,1\pm} = \pm \arccos \left[ \frac{-\tilde{J}_v + \sqrt{A(\tilde{J}_v^2 - 1 + A)}}{1 - A} \right], \quad (25)$$

and

$$k_{c,2\pm} = \pm \arccos \left[ \frac{-\tilde{J}_v - \sqrt{A(\tilde{J}_v^2 - 1 + A)}}{1 - A} \right], \quad (26)$$

with  $A = \sin \theta_i \sin \theta_f$ , which lead to the occurrence of a series of dynamical singularities of the rate function at

$$t_{n,1/2}^* = \frac{\pi}{2\epsilon_f(k_{c,1\pm/2\pm})} (2n - 1), \quad (27)$$

with

$$\epsilon_f(k_{c,1\pm/2\pm})/2J = \sqrt{(\sin \theta_f - \sin \theta_i) \sin \theta_f \sin^2 k_{c,1\pm/2\pm}} \quad (28)$$

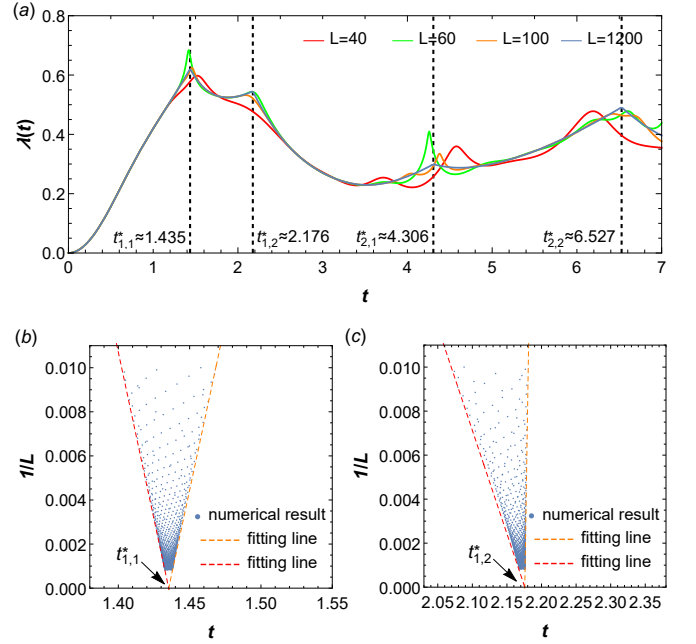


Figure 4. (a) The rate function  $\lambda(t)$  versus  $t$  for the Creutz model with different system sizes  $L = 40, 60, 100,$  and  $1200$ . Vertical dashed lines guide the values of critical times  $t_{1,1}^* \approx 1.435$ ,  $t_{1,2}^* \approx 2.176$ ,  $t_{2,1}^* \approx 4.306$ , and  $t_{2,2}^* \approx 6.527$ , respectively. (b), (c) are numerical results of the time when  $\lambda$  takes its local maximums for different sizes  $L$ . Here  $\tilde{J}_v = 0.5$ ,  $\theta_i = 0.4$ , and  $\theta_f = -0.4$ .

and  $n$  being a positive integer. Since  $\epsilon_f(k_{c,1+/2+}) = \epsilon_f(k_{c,1-/2-})$ , we omit the subscript  $\pm$  in  $t_{n,1/2}^*$ . Similarly,  $k_{c,1\pm}$  and  $k_{c,2\pm}$  are usually not equal to the quantized momentum values  $k = 2\pi m/L$  enforced by the PBC except for some fine-tuned postquench parameters. It means that the exact zeros of LE of a finite-size system generally do not exist for arbitrary  $\theta_i$  and  $\theta_f$ . With the increase in the system size,  $k_{c,1\pm/2\pm}$  can be approached in terms of  $\min |k - k_{c,1\pm/2\pm}| \leq \pi/L$ , and thus dynamical singularities of the rate function are usually only achieved in the limit of  $L \rightarrow \infty$ .

In Fig. 4(a), we display the rate function  $\lambda(t)$  versus time  $t$  for different system sizes  $L$ . From Figs. 4(b) and 4(c) we can see that  $t_{1,1}^*(L)$  and  $t_{1,2}^*(L)$  approach the critical times in an oscillating way as the size  $L$  increases. With the increase of the size  $L$ , we find that the value of  $\lambda_{\max}$  also approaches a finite number in an oscillating way and  $\lambda_{\max} \sim 0.621$  when  $L \rightarrow \infty$ . In the thermodynamical limit, the momentum  $k$  distributes continuously and we have  $\lambda(t) = -\frac{1}{2\pi} \int_0^{2\pi} \ln[1 - \Lambda_k \sin^2[\epsilon_f(k)t]] dk$ , from which we numerically evaluate the value  $\lambda(t_{1,1}^*) \approx 0.621$  at the critical time  $t_{1,1}^*$ , agreeing with  $\lambda_{\max}$  in the thermodynamical limit.

In Fig. 5(a), we exhibit the images of  $k_{c,1+}$ ,  $k_{c,1-}$ ,  $k_{c,2+}$ , and  $k_{c,2-}$  versus  $\theta_f$  for  $\theta_i = -0.4$  and  $\theta_i = 0.4$  according to Eqs. (25) and (26), and the four red circles denote  $k_{c,1\pm}/\pi \approx \pm 0.536$  and  $k_{c,2\pm}/\pi \approx \pm 0.772$  for

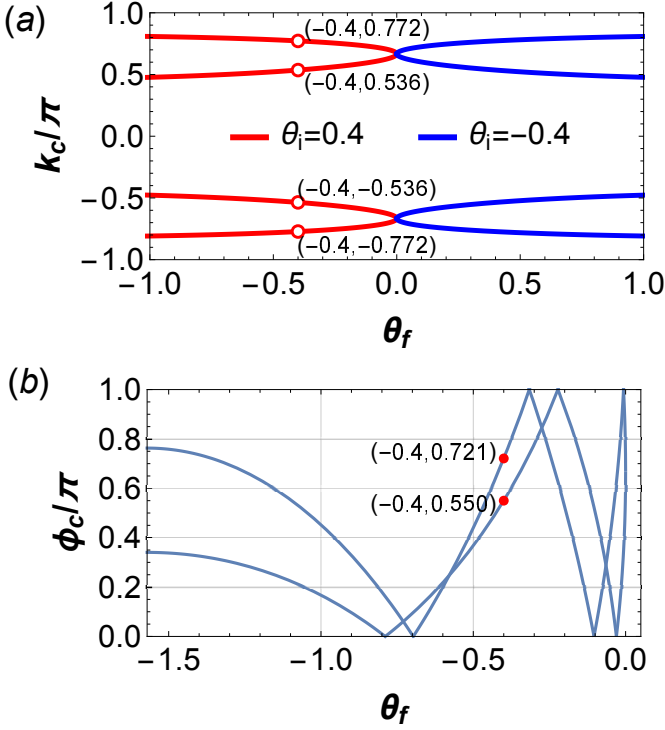


Figure 5. (a) The images of  $k_{c,1+}$ ,  $k_{c,1-}$ ,  $k_{c,2+}$ , and  $k_{c,2-}$  versus  $\theta_f$  for the Creutz model. The blue and red lines correspond to  $\theta_i = -0.4$  and  $\theta_i = 0.4$ , respectively. The four red circles denote  $k_{c,1\pm}/\pi \approx \pm 0.536$  and  $k_{c,2\pm}/\pi \approx \pm 0.772$  for  $\theta_i = 0.4$  and  $\theta_f = -0.4$ . (b) The exact solutions of  $\phi_{c,1}/\pi$  and  $\phi_{c,2}/\pi$  of the Creutz model for  $\theta_f \in [-\pi/2, 0]$ . The two red points denote  $\phi_{c,1}/\pi \approx 0.721$  and  $\phi_{c,2}/\pi \approx 0.550$  for  $\theta_f = -0.4$ . Here  $\theta_i = 0.4$ ,  $\tilde{J}_v = 0.5$ , and  $L = 20$ .

$\theta_i = 0.4$  and  $\theta_f = -0.4$ . Since the quantized momenta  $k$  usually do not include  $k_{c,1\pm}$  and  $k_{c,2\pm}$  under the PBC, we introduce the twist boundary condition here. For a system with a given finite size  $L$ , we can always achieve  $k_{c,1+/2+}$  or  $k_{c,1-/2-}$  by using the twist boundary condition with

$$\phi_{c,1/2} = \min\{\text{mod}[Lk_{c,1+/2+}, 2\pi], \text{mod}[Lk_{c,1-/2-}, 2\pi]\}. \quad (29)$$

Figure 5(b) displays the images of  $\phi_{c,1}/\pi$  and  $\phi_{c,2}/\pi$  versus  $\theta_f$  according to Eq. (29) for the system with  $\theta_i = 0.4$ ,  $\tilde{J}_v = 0.5$ , and  $L = 20$ , and the two red points denote  $\phi_{c,1}/\pi \approx 0.721$  and  $\phi_{c,2}/\pi \approx 0.550$  for  $\theta_i = 0.4$  and  $\theta_f = -0.4$ .

Let  $\Delta_{1/2} = \phi - \phi_{c,1/2}$ , at the time  $t = t_{n,1/2}^*$  we can get

$$\lambda(t_{n,1/2}^*) = -\frac{1}{L} \left[ \ln \mathcal{L}_{k_{1/2}^*}(t_{n,1/2}^*) + \sum_{k \neq k_{1/2}^*} \ln \mathcal{L}_k(t_{n,1/2}^*) \right], \quad (30)$$

where  $\mathcal{L}_{k_{1/2}^*}(t_{n,1/2}^*)$  comes from the contribution of the  $k_{1/2}^*$ -mode which is closest to  $k_{c,1/2}$ , i.e.,  $k_{1/2}^* = k_{c,1/2} +$

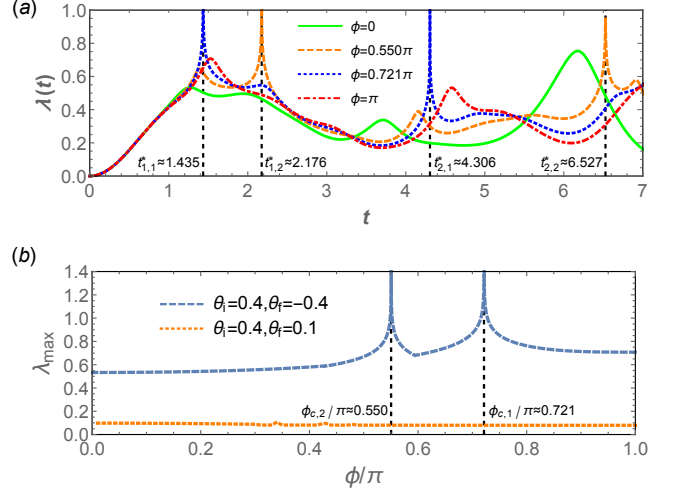


Figure 6. (a) The rate function  $\lambda(t)$  versus  $t$  for the Creutz model with  $\theta_i = 0.4$ ,  $\theta_f = -0.4$ ,  $\phi = 0, 0.550\pi, 0.721\pi$ , and  $\pi$ , respectively. Vertical dashed lines guide the divergent points  $t_{1,1}^* \approx 1.435$ ,  $t_{1,2}^* \approx 2.176$ ,  $t_{2,1}^* \approx 4.306$ , and  $t_{2,2}^* \approx 6.527$ . (b) The images of  $\lambda_{\max}$  versus  $\phi/\pi$ . The dashed blue line corresponds to  $\theta_i = 0.4$ ,  $\theta_f = -0.4$ , and the dotted orange line corresponds to  $\theta_i = 0.4$ ,  $\theta_f = 0.1$ . Vertical dashed lines guide the divergent points  $\phi_{c,1}/\pi \approx 0.721$  and  $\phi_{c,2}/\pi \approx 0.550$ . Here we take  $\tilde{J}_v = 0.5$  and  $L = 20$ .

$\Delta_{1/2}/L$ . Let  $\Delta_{1/2} \rightarrow 0$ , we can get

$$\mathcal{L}_{k_{1/2}^*}(t_{n,1/2}^*) \approx B_{1/2} \Delta_{1/2}^2, \quad (31)$$

where

$$B_{1/2} = \frac{4[t_{n,1/2}^{*2}(\tilde{J}_v + \cos k_{c,1/2} \cos^2 \theta_f)^2 - C]}{(\sin \theta_f - \sin \theta_i) \sin \theta_f L^2},$$

with  $C = \frac{\sin \theta_f (\tilde{J}_v^2 - 1 + \sin \theta_i \sin \theta_f)}{\sin^2 k_{c,1/2} (\sin \theta_f - \sin \theta_i)}$ . It means when  $\Delta_{1/2} \rightarrow 0$ , i.e.,  $\phi \rightarrow \phi_{c,1/2}$ ,  $\mathcal{L}_{k_{1/2}^*}(t_{n,1/2}^*) \propto \Delta_{1/2}^2$ . When  $\phi$  reaches  $\phi_{c,1/2}$ , we can get a  $k_{1/2}^*$ -mode which satisfies  $k_{1/2}^* = k_{c,1/2}$  and  $\mathcal{L}_{k_{1/2}^*}(t_{n,1/2}^*) = 0$ , thus the rate function is divergent at  $t_{n,1/2}^*$ .

In Fig. 6(a), we demonstrate rate functions versus  $t$  for various  $\phi$  with  $L = 20$ ,  $\tilde{J}_v = 0.5$ ,  $\theta_i = 0.4$ , and  $\theta_f = -0.4$ . It is shown that the rate functions are divergent at the critical times  $t_{1,1}^* \approx 1.435$  and  $t_{2,1}^* \approx 4.306$ , when  $\phi$  is tuned to the critical value  $\phi_{c,1} \approx 0.721\pi$ , and divergent at the critical times  $t_{1,2}^* \approx 2.176$  and  $t_{2,2}^* \approx 6.527$ , when  $\phi$  is tuned to the critical value  $\phi_{c,2} \approx 0.550\pi$ . In comparison with Fig. 4(a), all the nonanalytical behaviors occur at the same critical times obtained by finite-size-scaling analysis. For a pair of given  $\theta_i$  and  $\theta_f$ , Fig. 6(b) shows that if  $\theta_i$  and  $\theta_f$  belong to the same phase,  $\lambda_{\max}$  only changes slightly with  $\phi$ , which means the absence of DQPT; if  $\theta_i$  and  $\theta_f$  belong to different phases,  $\lambda_{\max}$  will diverge at  $\phi_{c,1}/\pi$  and  $\phi_{c,2}/\pi$ , indicating the occurrence of DQPT. It is a remarkable fact that there are two critical magnetic fluxes  $\phi_{c,1}$  and  $\phi_{c,2}$ , which are generated by

two pairs of momentum modes  $k_{c,1\pm}$  and  $k_{c,2\pm}$ , respectively. While  $\phi_{c,1}$  only produces singularities at  $t_{n,1}^*$ ,  $\phi_{c,2}$  produces singularities at  $t_{n,2}^*$ .

### III. APPLICATION TO OTHER MODEL SYSTEMS

To exhibit the applicability of our theoretical scheme to more general cases, here we study more examples by taking account into the effect long-range hopping, dimensionality, and interaction. We shall explore the dynamical singularity of rate function in the SSH model with long-range hopping, the two-dimensional Qi-Wu-Zhang model<sup>39</sup>, and the interacting SSH model, respectively.

#### A. SSH model with long-range hopping

Consider the SSH model with long-range hopping described by

$$H = \sum_{n=1}^L \sum_{r=1}^{L/2} (V_{1,r} c_{A,n}^\dagger c_{B,n+r-1} + V_{2,r} c_{A,n+r}^\dagger c_{B,n} + V_{3,r} c_{A,n}^\dagger c_{A,n+r} + V_{4,r} c_{B,n}^\dagger c_{B,n+r} + \text{H.c.}), \quad (32)$$

where  $V_{1,r} = J_1 e^{-\alpha(r-1)}$ ,  $V_{2,r} = J_2 e^{-\alpha(r-1)}$ ,  $V_{3,r} = J_3 e^{-\alpha(r-1)}$ ,  $V_{4,r} = J_4 e^{-\alpha(r-1)}$ , and  $\alpha$  is a tunable positive parameter. The model is schematically depicted in Fig. 7(a). By using the Fourier transformation  $c_{A/B,n}^\dagger = \frac{1}{\sqrt{L}} \sum_k e^{ikn} c_{A/B,k}^\dagger$ , we get

$$H = \sum_k \sum_{r=1}^{L/2} [(V_{1,r} e^{-ik(r-1)} + V_{2,r} e^{ikr}) c_{A,k}^\dagger c_{B,k} + \cos[kr] (V_{3,r} c_{A,k}^\dagger c_{A,k} + V_{4,r} c_{B,k}^\dagger c_{B,k}) + \text{H.c.}]. \quad (33)$$

The vector components of the Hamiltonian in momentum space are

$$d_x(k) = \sum_{r=1}^{L/2} (V_{1,r} \cos[k(r-1)] + V_{2,r} \cos[kr]), \quad (34)$$

$$d_y(k) = \sum_{r=1}^{L/2} (V_{1,r} \sin[k(r-1)] - V_{2,r} \sin[kr]), \quad (35)$$

$$d_z(k) = \sum_{r=1}^{L/2} (V_{3,r} - V_{4,r}) \cos[kr], \quad (36)$$

$$d_0(k) = \sum_{r=1}^{L/2} (V_{3,r} + V_{4,r}) \cos[kr]. \quad (37)$$

For simplicity, we set  $V_{3,r} = V_{4,r}$  and choose  $V_{2,r}$  as the quench parameter. The phase transition point is

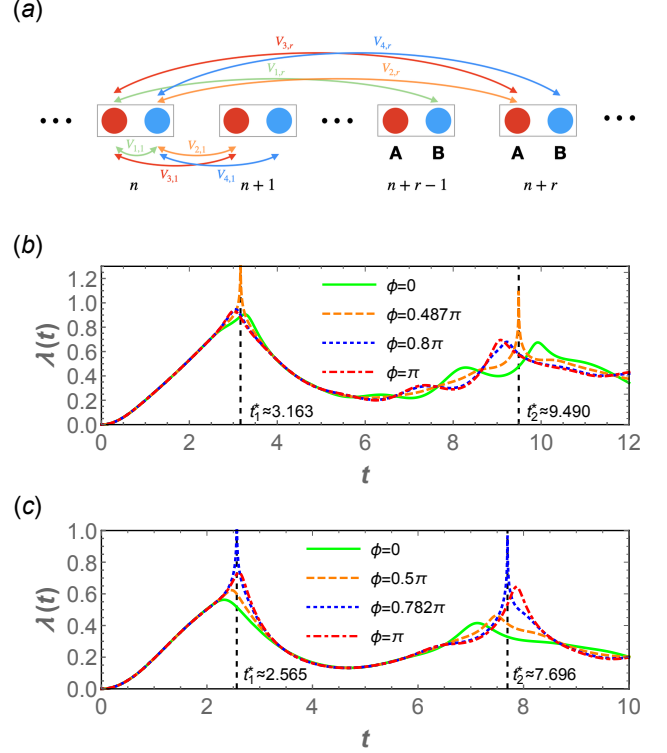


Figure 7. (a) A scheme for the SSH model with long-range hopping. (b) The rate function  $\lambda(t)$  versus  $t$  with  $\phi = 0, 0.487\pi, 0.8\pi$ , and  $\pi$  for the system with  $\alpha = 1$ , respectively. Vertical dashed lines guide the divergent points  $t_1^* \approx 3.163$  and  $t_2^* \approx 9.490$ . (c) The rate function  $\lambda(t)$  versus  $t$  with  $\phi = 0, 0.5\pi, 0.782\pi$ , and  $\pi$  for the system with  $\alpha = 10$ , respectively. Vertical dashed lines guide the divergent points  $t_1^* \approx 2.565$  and  $t_2^* \approx 7.696$ . Here we take  $J_1 = 1$ ,  $J_{2i} = 1.5$ ,  $J_{2f} = 0.5$ , and  $L = 20$ .

$V_{2c,r}/V_{1,r} = 1$ . According to Eq. (6), the corresponding constraint relation for the occurrence of divergence of the rate function is

$$\begin{aligned} & \sum_{r=1}^{L/2} (V_{1,r} \cos[k(r-1)] + V_{2i,r} \cos[kr]) \\ & \times \sum_{r=1}^{L/2} (V_{1,r} \cos[k(r-1)] + V_{2f,r} \cos[kr]) \\ & + \sum_{r=1}^{L/2} (V_{1,r} \sin[k(r-1)] - V_{2i,r} \sin[kr]) \\ & \times \sum_{r=1}^{L/2} (V_{1,r} \sin[k(r-1)] - V_{2f,r} \sin[kr]) = 0. \quad (38) \end{aligned}$$

If we choose  $J_1 = 1$ ,  $J_{2i} = 1.5$ ,  $J_{2f} = 0.5$ ,  $\alpha = 1$ , and  $L = 20$ , we can get  $k_c \approx 0.676\pi$  from Eq. (38). Then it follows that  $\phi_c \approx 0.487\pi$ ,  $t_1^* \approx 3.163$ , and  $t_2^* \approx 9.490$ . In Fig. 7(b), we show the image of rate function for the case of  $\alpha = 1$  with various  $\phi$ . It is obvious that the rate function diverges at  $t_1^*$  and  $t_2^*$  for  $\phi_c \approx 0.487\pi$ , while the rate

function is analytic for other values of  $\phi$ . As a comparison, we choose  $\alpha = 10$  and keep the other parameters the same as the case of  $\alpha = 1$ , and the rate function is displayed in Fig. 7(c). In this case, the amplitude of hopping decays rapidly so that the dynamical behavior of the model resembles the SSH model without long-range hopping. Similar to Fig. 3(a), the result for the case of  $\alpha = 10$  in Fig. 7(c) shows that the rate function diverges at  $t_1^* \approx 2.565$  and  $t_2^* \approx 7.696$  for  $\phi_c \approx 0.782\pi$ .

## B. Qi-Wu-Zhang model

Next we consider the Qi-Wu-Zhang model, which is a two-dimensional two-band model described by

$$\begin{aligned}
H = & -\frac{1}{2} \sum_{n_x, n_y} [(c_{n_x, n_y}^\dagger c_{n_x+1, n_y} + c_{n_x, n_y}^\dagger c_{n_x, n_y+1}) \\
& + i c_{n_x, n_y}^\dagger c_{n_x, n_y+1}^\dagger - c_{n_x, n_y}^\dagger c_{n_x+1, n_y}^\dagger \\
& + \mu c_{n_x, n_y}^\dagger c_{n_x, n_y} + \text{H.c.}], \quad (39)
\end{aligned}$$

where  $\mu$  is the chemical potential. After the Fourier transformation, we get the vector components of the Hamiltonian in momentum space as

$$d_x = \sin k_y, \quad (40)$$

$$d_y = -\sin k_x, \quad (41)$$

$$d_z = -\cos k_x - \cos k_y - \mu, \quad (42)$$

$$d_0 = -2\mu. \quad (43)$$

Depending on the value of  $\mu$ , the Qi-Wu-Zhang model is known to have three different topological phases characterized by different band Chern numbers with transition points at  $\mu_c = 0$  and  $\pm 2^{39}$ .

According to Eq. (6), the corresponding constraint relation for the occurrence of divergence of the rate function is

$$\mu_i \mu_f + (\cos k_x + \cos k_y)(\mu_i + \mu_f) + 2 \cos k_x \cos k_y + 2 = 0. \quad (44)$$

For the Qi-Wu-Zhang model, we find plenty of pairs of  $(k_{xc}, k_{yc})$  satisfy Eq. (44), and the value of  $k_{yc}$  is determined by

$$k_{yc} = \pm \arccos \left[ \frac{-\mu_i \mu_f - (\mu_i + \mu_f) \cos k_{xc} - 2}{\mu_i + \mu_f + 2 \cos k_{xc}} \right]. \quad (45)$$

Taking  $\mu$  as the quench parameter, we choose  $\mu_i \in (0, 2)$  and  $\mu_f \in (-2, 0)$ . To make sure that  $k_{yc}$  is real, the value of  $k_{xc}$  is bounded as follows:

$$\begin{aligned}
\cos k_{xc} \in & \left[ -1, -\frac{\mu_i \mu_f}{\mu_i + \mu_f + 2} - 1 \right] \\
& \cup \left[ -\frac{\mu_i \mu_f}{\mu_i + \mu_f - 2} + 1, 1 \right]. \quad (46)
\end{aligned}$$

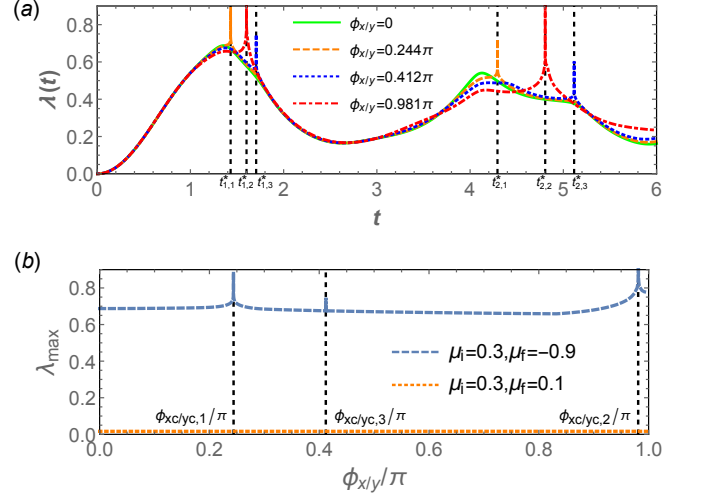


Figure 8. (a) The rate function  $\lambda(t)$  versus  $t$  for the Qi-Wu-Zhang model with  $\mu_i = 0.3$ ,  $\mu_f = -0.9$ ,  $\phi_{x/y} = 0, 0.244\pi, 0.412\pi$ , and  $0.981\pi$ , respectively. Vertical dashed lines guide the divergent points  $t_{1,1}^* \approx 1.431$ ,  $t_{1,2}^* \approx 1.602$ ,  $t_{1,3}^* \approx 1.705$ ,  $t_{2,1}^* \approx 4.294$ ,  $t_{2,2}^* \approx 4.805$ , and  $t_{2,3}^* \approx 5.116$ . (b) The images of  $\lambda_{\max}$  versus  $\phi_{x/y}/\pi$ . The dashed blue line corresponds to  $\mu_i = 0.3$ ,  $\mu_f = -0.9$ , and the dotted orange line corresponds to  $\mu_i = 0.3$ ,  $\mu_f = 0.1$ . Vertical dashed lines guide the divergent points  $\phi_{xc/yc,1}/\pi \approx 0.244$ ,  $\phi_{xc/yc,3}/\pi \approx 0.412$ , and  $\phi_{xc/yc,2}/\pi \approx 0.981$ . Here we take  $L_x = L_y = 12$ .

It should be noted that the critical time  $t_n^*$  is no longer a value, but in a region:

$$t_n^* \in \left[ \frac{(2n-1)\pi}{2\sqrt{\frac{\mu_f(\mu_f-2)(\mu_f-\mu_i)}{\mu_i+\mu_f-2}}}, \frac{(2n-1)\pi}{2\sqrt{\frac{\mu_f(\mu_f+2)(\mu_f-\mu_i)}{\mu_i+\mu_f+2}}} \right], \quad (47)$$

where  $n$  is a positive integer.

It is worth noting that, for a finite-size system, both  $k_x$  and  $k_y$  take discrete values. Thus the number of pairs of  $(k_{xc}, k_{yc})$  satisfying Eq. (44) is finite. If we choose  $\mu_i = 0.3$ ,  $\mu_f = -0.9$ , and  $L_x = L_y = 12$ , we can get 16 pairs of  $(k_{xc}, k_{yc})$  from Eq. (44), given by  $(k_{xc,1}, k_{yc,1}) \approx (\pm 0.146\pi, \pi)$  or  $(\pi, \pm 0.146\pi)$ ,  $(k_{xc,2}, k_{yc,2}) \approx (\pm 0.0849\pi, \pm 5\pi/6)$  or  $(\pm 5\pi/6, \pm 0.0849\pi)$ , and  $(k_{xc,3}, k_{yc,3}) \approx (\pm 0.799\pi, 0)$  or  $(0, \pm 0.799\pi)$ . By applying the twist boundary conditions  $(k_x = \frac{2\pi m_x + \phi_{xc}}{L_x}, k_y = \frac{2\pi m_y}{L_y})$  or  $(k_x = \frac{2\pi m_x}{L_x}, k_y = \frac{2\pi m_y + \phi_{yc}}{L_y})$  with  $\phi_{xc/yc,1} \approx 0.244\pi$ ,  $\phi_{xc/yc,2} \approx 0.981\pi$ , and  $\phi_{xc/yc,3} \approx 0.412\pi$ , we get the corresponding critical times given by  $t_{n,1}^* \approx 1.431(2n-1)$ ,  $t_{n,2}^* \approx 1.602(2n-1)$ , and  $t_{n,3}^* \approx 1.705(2n-1)$ , respectively. In Fig. 8(a), we show the image of the rate function for the Qi-Wu-Zhang model for various  $\phi_{x/y}$ , where  $\mu_i = 0.3$ ,  $\mu_f = -0.9$  and  $L_x = L_y = 12$ . The rate functions distinctly diverge at the corresponding critical times for  $\phi_{x/y} = \phi_{xc/yc,1}$ ,  $\phi_{x/y} = \phi_{xc/yc,2}$ , and  $\phi_{x/y} = \phi_{xc/yc,3}$ ,



while the rate function under the period boundary condition is smooth for all time. Figure 8(b) exhibits that  $\lambda_{\max}$  diverges at  $\phi_{xc/yc,1} \approx 0.244\pi$ ,  $\phi_{xc/yc,2} \approx 0.981\pi$ , and  $\phi_{xc/yc,3} \approx 0.412\pi$  when  $\mu_i$  and  $\mu_f$  are in different phase regions, while there is no divergence when  $\mu_i$  and  $\mu_f$  belong to the same phase. It is important to note that each  $\phi_{xc/yc}$  just produces a part of all the singularities. To obtain the whole critical times  $t_1^* \in [1.431, 1.705]$ ,  $t_2^* \in [4.294, 5.116]$ , and so on, one needs to add proper twist boundary conditions on both the  $x$  and  $y$  directions simultaneously.

### C. Interacting SSH model

To check whether our theoretical scheme works for the interacting system, now we consider the interacting SSH model with the twist boundary condition,

$$\begin{aligned}
 H = & \sum_{j=1}^{L-1} \left( J_1 c_{j,A}^\dagger c_{j,B} + J_2 c_{j,B}^\dagger c_{j+1,A} + \text{H.c.} \right) \\
 & + \left( J_1 c_{L,A}^\dagger c_{L,B} + J_2 e^{-i\phi} c_{L,B}^\dagger c_{1,A} + \text{H.c.} \right) \\
 & + U \sum_{j=1}^L (n_{j,A} n_{j,B} + n_{j,B} n_{j+1,A}), \quad (48)
 \end{aligned}$$

where  $U > 0$  characterizes the strength of the nearest-neighbor repulsive interaction,  $n_{j,A/B}$  denotes the fermion occupation number operator of sublattice  $A/B$  on the unit cell  $j$ , and  $n_{L+1,A} = n_{1,A}$ . Here we shall consider the half-filling case. The topological phase transition of the interacting SSH model under the periodic boundary condition was discussed in Ref.<sup>40</sup>. When  $U$  is much larger than  $J_1$  and  $J_2$ , the system is in a density-wave phase with the ground state approximately described by  $|1010 \dots\rangle$  or  $|0101 \dots\rangle$ . Here we shall consider the case with  $U$  much smaller than  $J_1$  and  $J_2$ , for which there is still a phase transition when we change the parameter  $J_2/J_1$  with the transition point close to  $J_2/J_1 = 1$  when  $U$  is small.

Since our motivation is to observe the signature of dynamical singularity in a small size system, we shall not pursue determining the phase boundary of the system precisely. By applying the finite-size scaling of fidelity<sup>40</sup>, we obtain the approximate value of the phase transition point  $J_{2c}/J_1 \approx 1.038$  and  $J_{2c}/J_1 \approx 1.103$  for  $U = 0.1$  and  $U = 0.6$ , respectively. We numerically calculate the rate function by exact diagonalization of a system with  $L = 5$  by fixing  $U$  and  $J_1 = 1$  and quenching the parameter  $J_2$ . The numerical results are shown in Fig. 9. For quench from  $J_2/J_1 < 1$  to  $J_2/J_1 > 1$ , we can observe that the rate functions present some peaks at some typical magnetic fluxes  $\phi$ , as shown in Figs. 9(c) and 9(d). However, these peaks are absent for the quench process from  $J_2/J_1 < 1$  to  $J_2/J_1 < 1$ , as shown in Figs. 9(a) and 9(b). By scrutinizing these peaks in Figs. 9(c) and 9(d), we choose three rate functions from Figs. 9(c) and 9(d)

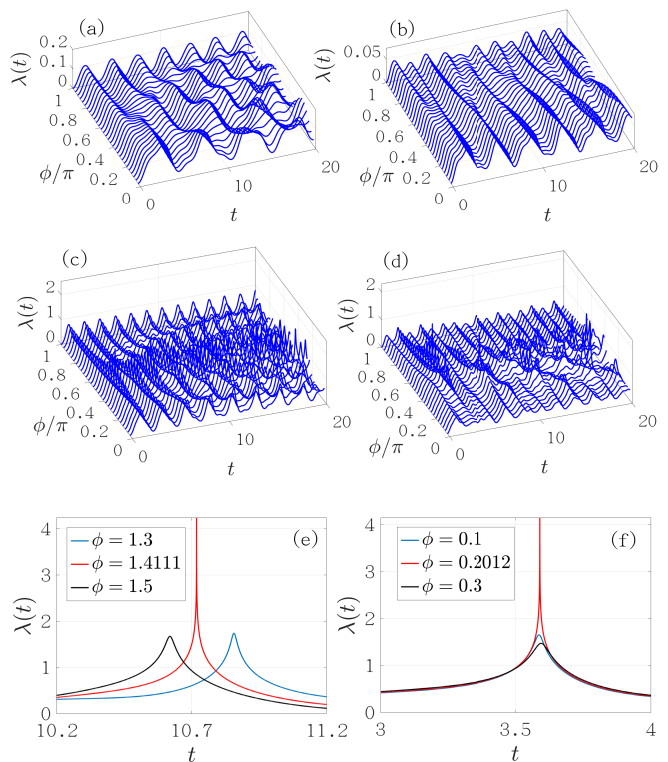


Figure 9. The rate function  $\lambda(t)$  versus  $t$  for the interacting SSH model with  $J_1 = 1, J_{2i} = 0.2$ , and  $L = 5$ . The other parameters are (a)  $U = 0.1, J_{2f} = 0.7$ ; (b)  $U = 0.6, J_{2f} = 0.7$ ; (c),(e)  $U = 0.1, J_{2f} = 2$ ; (d),(f)  $U = 0.6, J_{2f} = 2$ .

and show them in Figs. 9(e) and 9(f), respectively. We can see that the rate function with  $\phi = 1.4111$  in Fig. 9(e) and the rate function with  $\phi = 0.2012$  in Fig. 9(f) exhibit obvious peaks, while the other four rate functions display no divergence. Our numerical results indicate a clear signature of dynamical singularity even in a small size interacting system by tuning the magnetic flux.

## IV. CONCLUSION AND DISCUSSION

In summary, we proposed a theoretical scheme for studying the dynamical singularity of the rate function in finite-size quantum systems which exhibit DQPT in the thermodynamic limit. The dynamical singularity of the rate function occurs whenever the corresponding LE has exact zero points, which is, however, not accessible in a finite-size quantum system with the PBC because the momentum takes quantized values  $k = 2\pi m/L$ . To realize the exact zeros of LE, we consider the twist boundary condition by applying a magnetic flux into the system, which enables us to shift the quantized momentum continuously to achieve the exact zeros of LE. Taking the SSH model and Creutz model as concrete examples, we demonstrate that tuning the magnetic flux can lead to

the occurrence of divergency in the rate function of a finite-size system at the same critical times as in the case of the thermodynamical limit, when the quench parameter is across the underlying equilibrium phase transition point. We also exhibit the applicability of our theoretical scheme to more general cases, including the SSH model with long-range hopping, the Qi-Wu-Zhang model, and the interacting SSH model.

Our work unveils that the singularity of the rate function is accessible in finite-size quantum systems by introducing an additional magnetic flux, which provides a possible way for experimentally detecting DQPT and the critical times in finite-size quantum systems. For the experimental setup in a trapped-ion quantum simulator<sup>26,27</sup>, it remains a challenging task to create tunable magnetic flux in the setup. However, for the

cold atomic system, one can implement discrete momentum states by using multifrequency Bragg lasers to realize the SSH model on a momentum lattice<sup>41</sup>, where the synthetic magnetic flux through the ring are tunable<sup>42</sup>. We expect that the momentum lattice of cold atomic systems might be a promising platform to observe the dynamical singularity of the rate function related to the DQPT.

## ACKNOWLEDGMENTS

The work is supported by the National Key Research and Development Program of China (Grant No. 2021YFA1402104), the NSFC under Grants No.12174436 and No.T2121001, and the Strategic Priority Research Program of Chinese Academy of Sciences under Grant No. XDB33000000.

- 
- \* Corresponding author: schen@iphy.ac.cn
- <sup>1</sup> M. Heyl, A. Polkovnikov, S. Kehrein, Dynamical Quantum Phase Transitions in the Transverse-Field Ising Model, *Phys. Rev. Lett.* **110**, 135704 (2013).
  - <sup>2</sup> C. Karrasch and D. Schuricht, Dynamical phase transitions after quenches in nonintegrable models, *Phys. Rev. B* **87**, 195104 (2013).
  - <sup>3</sup> J. M. Hickey, S. Genway, and J. P. Garrahan, Dynamical phase transitions, time-integrated observables, and geometry of states, *Phys. Rev. B* **89**, 054301 (2014).
  - <sup>4</sup> E. Canovi, P. Werner, and M. Eckstein, First-Order Dynamical Phase Transitions, *Phys. Rev. Lett.* **113**, 265702 (2014).
  - <sup>5</sup> F. Andraschko and J. Sirker, Dynamical quantum phase transitions and the Loschmidt echo: A transfer matrix approach, *Phys. Rev. B* **89**, 125120 (2014).
  - <sup>6</sup> M. Schmitt and S. Kehrein, Dynamical quantum phase transitions in the Kitaev honeycomb model, *Phys. Rev. B* **92**, 075114 (2015).
  - <sup>7</sup> M. Heyl, Dynamical Quantum Phase Transitions in Systems with Broken-Symmetry Phases, *Phys. Rev. Lett.* **113**, 205701 (2014).
  - <sup>8</sup> M. Heyl, Scaling and Universality at Dynamical Quantum Phase Transitions, *Phys. Rev. Lett.* **115**, 140602 (2015).
  - <sup>9</sup> S. Vajna and B. Dóra, Topological classification of dynamical phase transitions, *Phys. Rev. B* **91**, 155127 (2015).
  - <sup>10</sup> J. C. Budich and M. Heyl, Dynamical topological order parameters far from equilibrium, *Phys. Rev. B* **93**, 085416 (2016).
  - <sup>11</sup> C. Yang, L. Li, and S. Chen, Dynamical topological invariant after a quantum quench, *Phys. Rev. B* **97**, 060304(R) (2018).
  - <sup>12</sup> B. Mera, C. Vlachou, N. Paunković, V. R. Vieira, and O. Viyuela, Dynamical phase transitions at finite temperature from fidelity and interferometric Loschmidt echo induced metrics, *Phys. Rev. B* **97**, 094110 (2018).
  - <sup>13</sup> S. Vajna and B. Dóra, Disentangling dynamical phase transitions from equilibrium phase transitions, *Phys. Rev. B* **89**, 161105(R) (2014).
  - <sup>14</sup> S. Sharma, S. Suzuki, and A. Dutta, Quenches and dynamical phase transitions in a nonintegrable quantum Ising model, *Phys. Rev. B* **92**, 104306 (2015).
  - <sup>15</sup> B. Zhou, C. Yang, and S. Chen, Signature of a nonequilibrium quantum phase transition in the long-time average of the Loschmidt echo, *Phys. Rev. B* **100**, 184313 (2019).
  - <sup>16</sup> G. Sun and B.-B. Wei, Dynamical quantum phase transitions in a spin chain with deconfined quantum critical points, *Phys. Rev. B* **102**, 094302 (2020).
  - <sup>17</sup> J. C. Halimeh and V. Zauner-Stauber, Dynamical phase diagram of spin chains with long-range interactions, *Phys. Rev. B* **96**, 134427 (2017).
  - <sup>18</sup> I. Homrighausen, N. O. Abeling, V. Zauner-Stauber, and J. C. Halimeh, Anomalous dynamical phase in quantum spin chains with long-range interactions, *Phys. Rev. B* **96**, 104436 (2017).
  - <sup>19</sup> R. Jafari and A. Akbari, Floquet dynamical phase transition and entanglement spectrum, *Phys. Rev. A* **103**, 012204 (2021).
  - <sup>20</sup> A. A. Zvyagin, Dynamical quantum phase transitions (Review Article), *Fiz. Nizk. Temp. (Kiev)* **42**, 1240 (2016) [*Low Temp. Phys.* **42**, 971 (2016)].
  - <sup>21</sup> M. Heyl, Dynamical quantum phase transitions: a review, *Rep. Prog. Phys.* **81**, 054001 (2018).
  - <sup>22</sup> T. Gorin, T. Prosen, T. H. Seligman, and M. Znidaric, Dynamics of Loschmidt echoes and fidelity decay, *Phys. Rep.* **435**, 33 (2006).
  - <sup>23</sup> D. Liska and V. Gritsev, The Loschmidt Index, *SciPost Phys.* **10**, 100 (2021).
  - <sup>24</sup> B. Zhou, Y. Zeng, and S. Chen, Exact zeros of the Loschmidt echo and quantum speed limit time for the dynamical quantum phase transition in finite-size systems, *Phys. Rev. B* **104**, 094311 (2021).
  - <sup>25</sup> P. W. Anderson, Infrared Catastrophe in Fermi Gases with Local Scattering Potentials, *Phys. Rev. Lett.* **18**, 1049 (1967).
  - <sup>26</sup> P. Jurcevic, H. Shen, P. Hauke, C. Maier, T. Brydges, C. Hempel, B. P. Lanyon, M. Heyl, R. Blatt, and C. F. Roos, Direct Observation of Dynamical Quantum Phase Transitions in an Interacting Many-Body System, *Phys. Rev. Lett.* **119**, 080501 (2017).
  - <sup>27</sup> J. Zhang, G. Pagano, P.W. Hess, A. Kyprianidis, P. Becker, H. Kaplan, A. V. Gorshkov, Z.-X. Gong, and C.

- Monroe, Observation of a many-body dynamical phase transition with a 53-qubit quantum simulator, *Nature (London)* **551**, 601 (2017).
- <sup>28</sup> H. Bernien, S. Schwartz, A. Keesling, H. Levine, A. Omran, H. Pichler, S. Choi, A. S. Zibrov, M. Endres, M. Greiner, V. Vuletic, and M. D. Lukin, Probing many-body dynamics on a 51-atom quantum simulator, *Nature (London)* **551**, 579 (2017).
- <sup>29</sup> N. Fläschner, D. Vogel, M. Tarnowski, B. S. Rem, D.-S. Lühmann, M. Heyl, J. C. Budich, L. Mathey, K. Sengstock, and C. Weitenberg, Observation of dynamical vortices after quenches in a system with topology, *Nat. Phys.* **14**, 265 (2018).
- <sup>30</sup> T. Tian, H.-X. Yang, L.-Y. Qiu, H.-Y. Liang, Y.-B. Yang, Y. Xu, and L.-M. Duan, Observation of Dynamical Quantum Phase Transitions with Correspondence in an Excited State Phase Diagram, *Phys. Rev. Lett.* **124**, 043001 (2020).
- <sup>31</sup> S. Smale, P. He, B. A. Olsen, K. G. Jackson, H. Sharum, S. Trotzky, J. Marino, A. M. Rey, and J. H. Thywissen, Observation of a transition between dynamical phases in a quantum degenerate fermi gas, *Sci. Adv.* **5**, eaax1568 (2019).
- <sup>32</sup> X.-Y. Guo, C. Yang, Y. Zeng, Y. Peng, H.-K. Li, H. Deng, Y.-R. Jin, S. Chen, D. Zheng, and H. Fan, Observation of a dynamical quantum phase transition by a superconducting qubit simulation, *Phys. Rev. Applied* **11**, 044080 (2019).
- <sup>33</sup> K. Wang, X. Qiu, L. Xiao, X. Zhan, Z. Bian, W. Yi, and P. Xue, Simulating Dynamic Quantum Phase Transitions in Photonic Quantum Walks, *Phys. Rev. Lett.* **122**, 020501 (2019).
- <sup>34</sup> W. P. Su, J. R. Schrieffer, and A. J. Heeger, Solitons in Polyacetylene, *Phys. Rev. Lett.* **42**, 1698 (1979).
- <sup>35</sup> M. Creutz, End States, Ladder Compounds, and Domain-Wall Fermions, *Phys. Rev. Lett.* **83**, 2636 (1999).
- <sup>36</sup> L. Li, Z. Xu, and S. Chen, Topological phases of generalized Su-Schrieffer-Heeger models, *Phys. Rev. B* **89**, 085111 (2014).
- <sup>37</sup> R. Jafari, H. Johannesson, A. Langari, and M. A. Martin-Delgado, Quench dynamics and zero-energy modes: The case of the Creutz model, *Phys. Rev. B* **99**, 054302 (2019).
- <sup>38</sup> Linhu Li and Shu Chen, Characterization of topological phase transitions via topological properties of transition points, *Phys. Rev. B* **92**, 085118 (2015).
- <sup>39</sup> X. Qi, Y. Wu, and S. Zhang, Topological quantization of the spin Hall effect in two-dimensional paramagnetic semiconductors, *Phys. Rev. B* **74**, 085308 (2006).
- <sup>40</sup> H.-K. Tang, M. A. Marshali, and W. C. Yu, Unveiling quantum phase transitions by fidelity mapping, *Phys. Rev. B* **104**, 075142 (2021).
- <sup>41</sup> D. Xie, W. Gou, T. Xiao, B. Gadway and B. Yan, Topological characterizations of an extended Su-Schrieffer-Heeger model, *Npj Quantum Inf.* **5**, 55 (2019).
- <sup>42</sup> W. Gou, T. Chen, D. Xie, T. Xiao, T.-S. Deng, B. Gadway, W. Yi, and B. Yan, Tunable Nonreciprocal Quantum Transport through a Dissipative Aharonov-Bohm Ring in Ultracold Atoms, *Phys. Rev. Lett.* **124**, 070402 (2020).